Perovskite oxides for application in thermochemical air separation and oxygen storage

Supporting Information

Josua Vieten,[#] Brendan Bulfin,[#] Friedemann Call,[#] Matthias Lange,[#] Martin Schmücker,[†] Alexander Francke,[†] Martin Roeb,*[#] and Christian Sattler.[#]

[#]Institute of Solar Research, *and* [†]Institute of Materials Research, Deutsches Zentrum für Luft- und Raumfahrt/German Aerospace Center—DLR, Linder Höhe, 51147 Köln, Germany.

1. Perovskite synthesis using the citric acid auto-combustion route

All perovskite materials were prepared using a citric acid auto-combustion route. 0.1 M aqueous solutions of calcium nitrate tetrahydrate (99 %, Alfa Aeasar), manganese(II)-nitrate tetrahydrate (for analysis, Acros Organics), iron(III)-nitrate nonahydrate (99.0 – 101.0 %, VWR Chemicals), and copper(II)-nitrate hemipentahydrate (98 %, Sigma Aldrich) were prepared and mixed according to the intended stoichiometry, resulting in about 50-100 mL of solution. Typically, 4-5 mmol of material were prepared, corresponding to a theoretical final mass of about 700-1000 mg of the perovskite. The mixtures were heated to their boiling point under continuous stirring and 4-5 mL of 5 M citric acid (99 %, Merck) in aqueous solution were added as a fuel for the following auto-combustion, corresponding to a fuel to oxidant (nitrate) ratio not smaller than 2. For availability reasons, strontium carbonate (99.99 %, Alfa Aeasar) was used as Sr source instead of the corresponding nitrate. The carbonate was added to the hot nitrate-acid mixture, and readily dissolved under the formation of CO_2 gas. After most of the water has been removed by evaporation, a viscous gel formed (see FIGURE 2 in main article), which was then further dried at 130 °C. The temperature was gradually increased to 200 °C in steps of 10 °C within 15–20 min to remove the remaining water and partially decompose citric acid. The gelation and decomposition process often induced a massive volume increase. Subsequently, the dried gels with low density were heated to 300–500 °C until ignition occurred, which was in many cases accompanied by a flash-like flame of

burning gaseous excess organic matter. The resulting oxide powders were then calcined in alumina crucibles in three steps under air at 800 °C (2 x 10 h) and 1300 °C (1 x 20 h). No intermediate mixing or powdering was carried out. The temperature program for calcination is displayed in FIGURE S1.

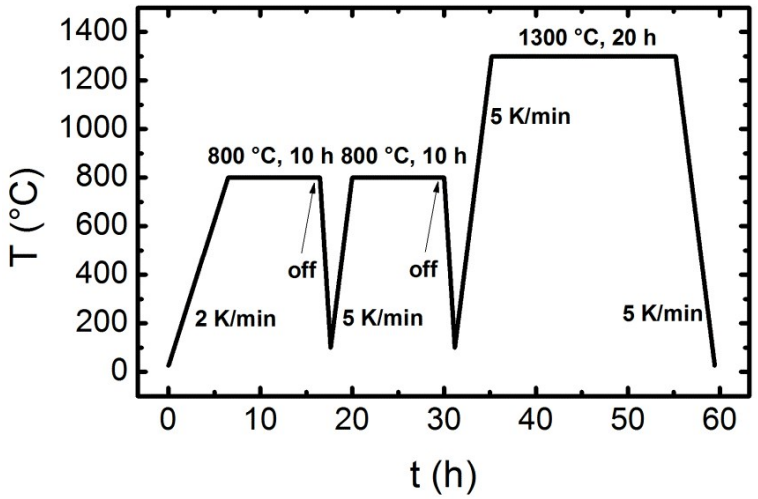

Fig. S1: Temperature program for perovskite synthesis from powder mixtures prepared using the citric acid auto-combustion method. After turning the furnace off in the two 800 °C steps, the system was given 4 h to cool down naturally before the next heating step.

2. XRD patterns and refinement; further thermogravimetric data

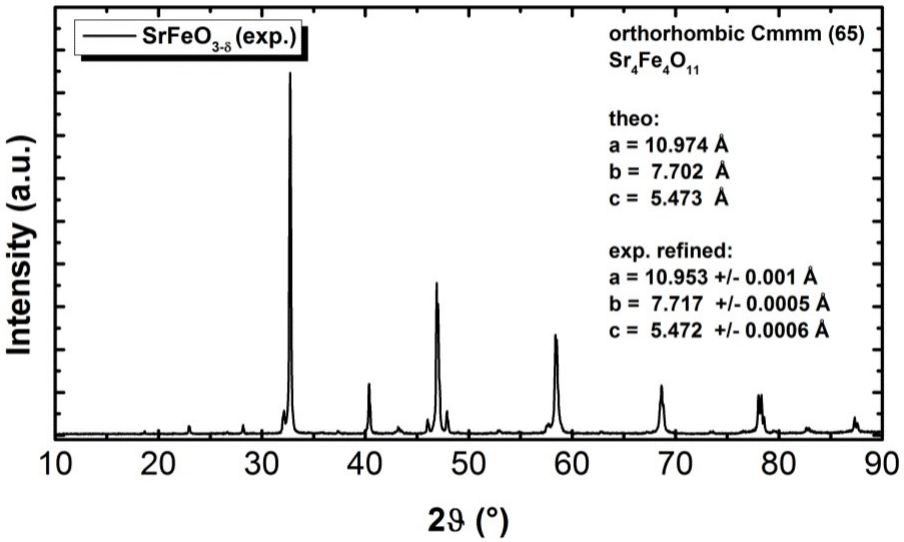

Fig. S2. Powder X-Ray diffraction pattern of $SrFeO_x$ after synthesis. Refinement performed in space group 65 with cif file No. 1521171[1] from the *Crystallography Open Database*. The refined cell parameters show deviations from the theoretical values, which may be attributed to the different oxygen stoichiometry.

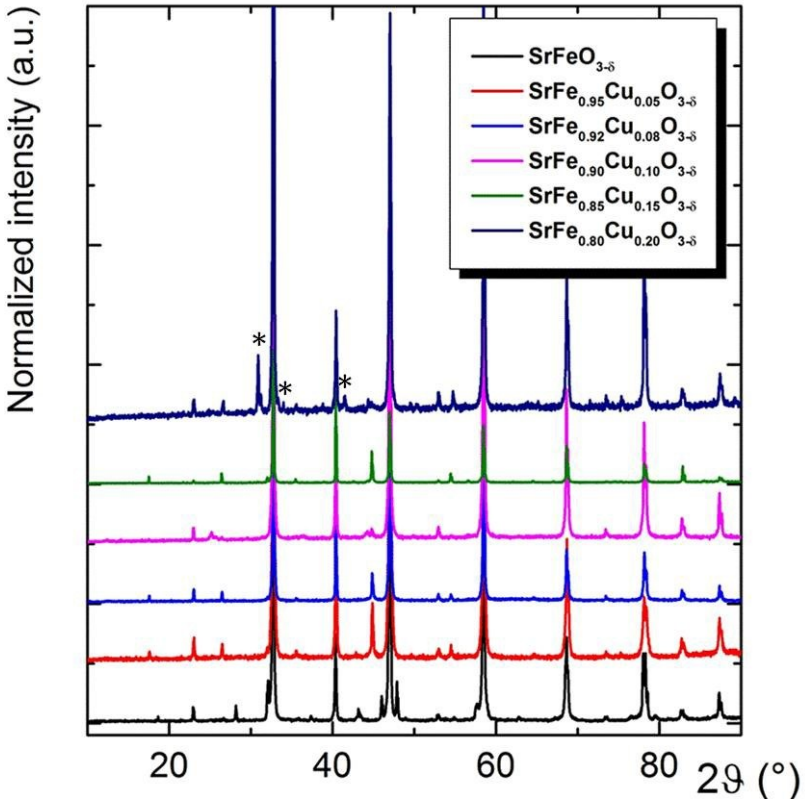

Fig. S3: Powder XRD patterns of Cu-doped $SrFeO_x$ at different doping levels and undoped $SrFeO_x$ for comparison. The $SrFe_{0.80}CuO_x$ phase shows additional reflections at 31°, 33°, and 41°, of which the first two at 31° and 33° might correspond to $Sr_2CuO_{4-\delta}$. [2, 3]

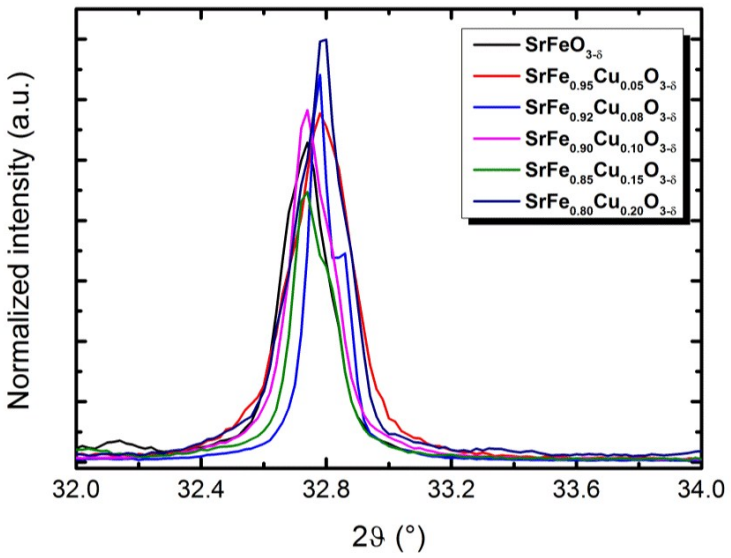

Fig. S4: Detailed view of XRD patterns of Cu-doped $SrFeO_x$ at different doping levels with undoped $SrFeO_x$ for comparison. The positions of the reflections remain essentially unchanged by doping.

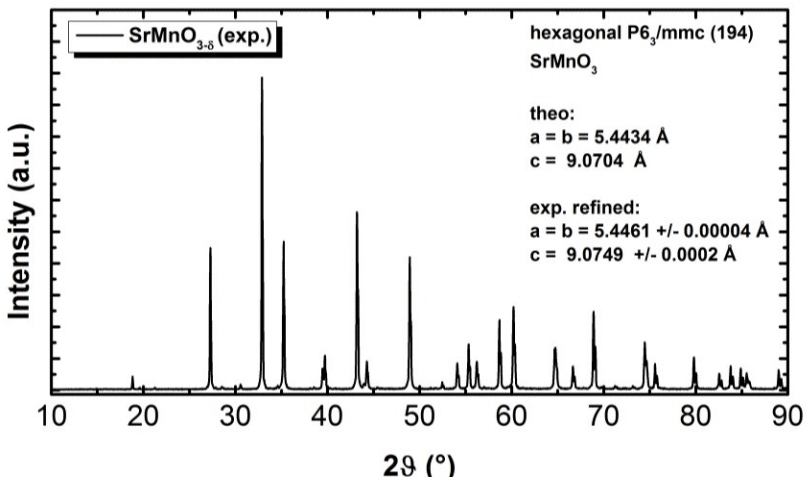

Fig. S5: Powder X-Ray diffraction pattern of $SrMnO_x$ after synthesis. Refinement performed in the hexagonal space group 194 with cif file No. 1529598 [4] from the *Crystallography Open Database*. The refined cell parameters are almost identical to values in literature [4].

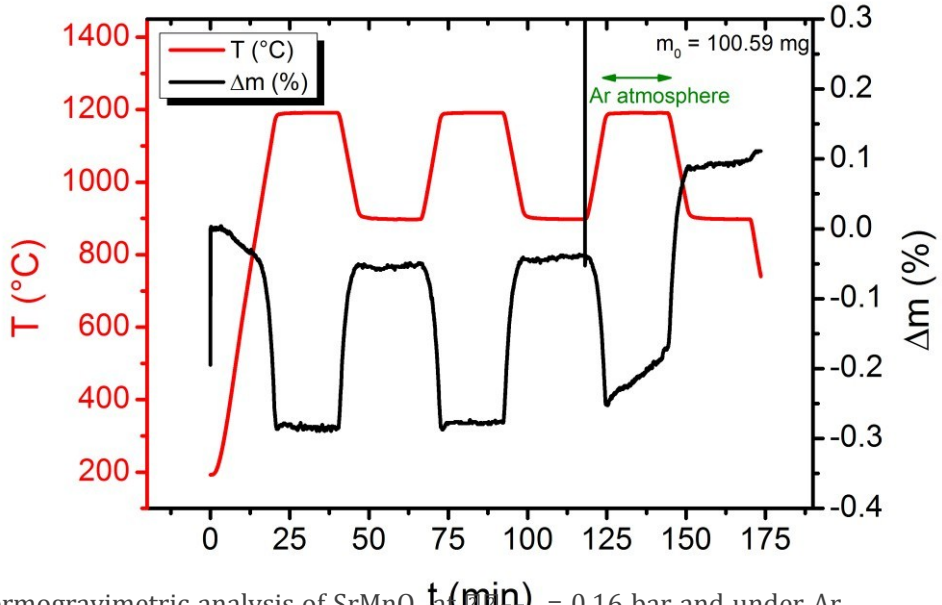

Fig. S6: Thermogravimetric analysis of $SrMnO_x$ at p_{O_2} = 0.16 bar and under Ar 5.0.

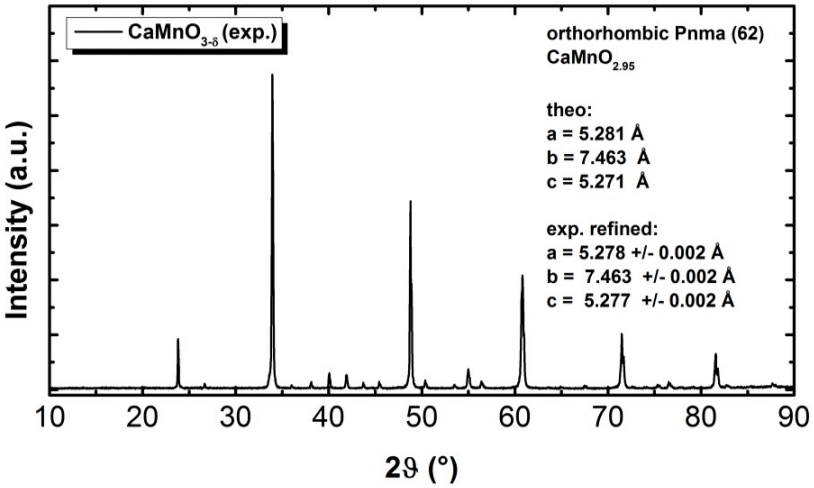

Fig. S7: Powder X-Ray diffraction pattern of $CaMnO_x$ after synthesis. Refinement performed in space group 62 with cif file No. 1525994 [5] from the *Crystallography Open Database*. **b.** Experimental diffraction pattern in combination with theoretical patterns from the *ICDD® PDF-2* database.

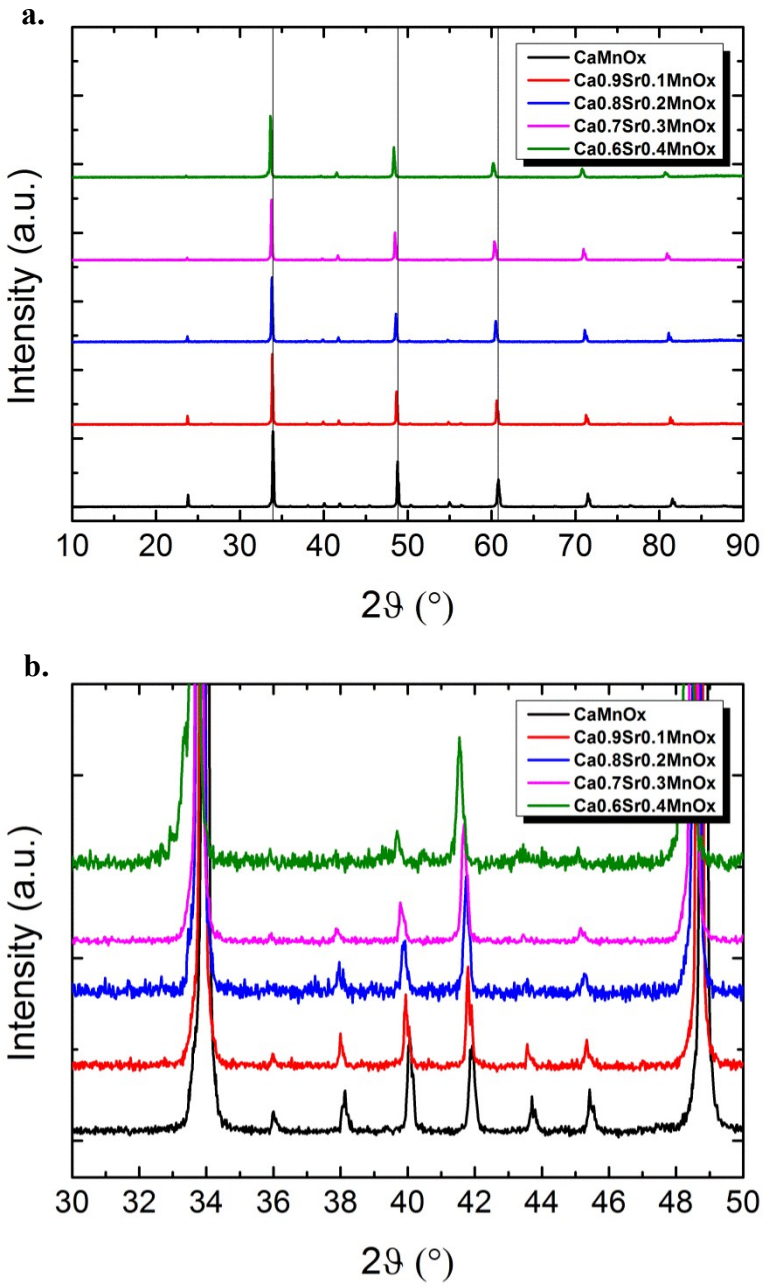

Fig. S8: X-Ray diffractograms of Sr-doped $CaMnO_x$ at different doping levels. **a.** The shift of reflections towards lower 2 ϑ values indicates the lattice expansion due to the incorporation of Sr into the lattice. **b.** The decreasing intensity of small reflections with increasing Sr content might indicate a lower distortion of the ideal cubic structure.

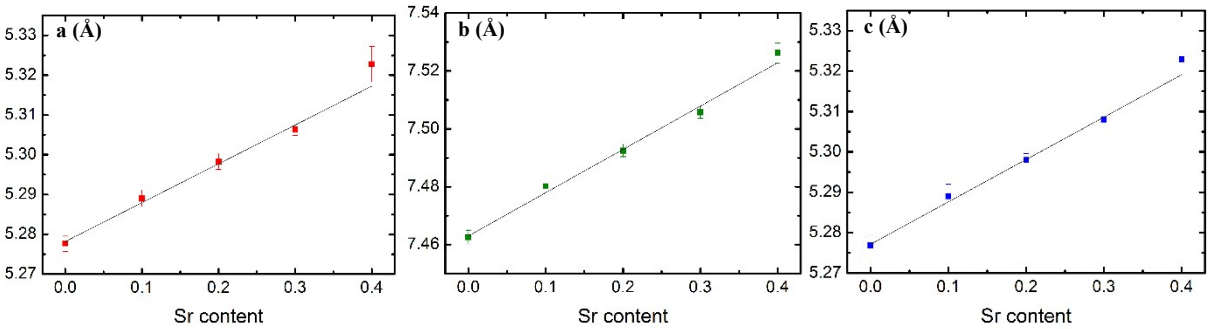

Fig. S9: Cell parameters of Sr-doped $CaMnO_x$ obtained via refinement in space group 62 using cif file No. 1525994 [5] from the *Crystallography Open Database*. The linear relationship between Sr content and lattice expansion is in good agreement with Vegard's law.

3. Long term studies and microstructure

$SrFe_{0.95}Cu_{0.05}O_x$

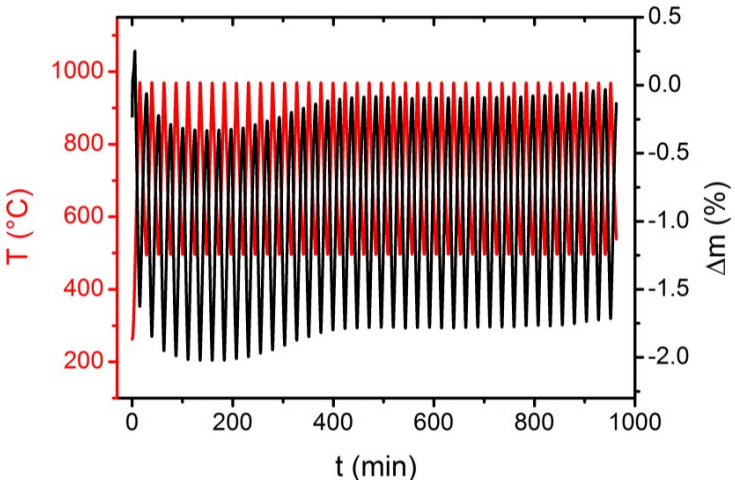

Fig. S10: Long term thermogravimetric experiment of $SrFe_{0.95}Cu_{0.05}O_x$ at p_{O_2} = 0.16 bar. 40 redox cycles were carried out. Drift corrected linearly, no empty scan subtracted. Initial sample mass:

90.08 mg. The sample was oxidized and reduced 10 times in previous experiments beforehand without any change of the redox activity. The observed non-linear drift was not corrected. The mass changes are virtually equal throughout all redox cycles.

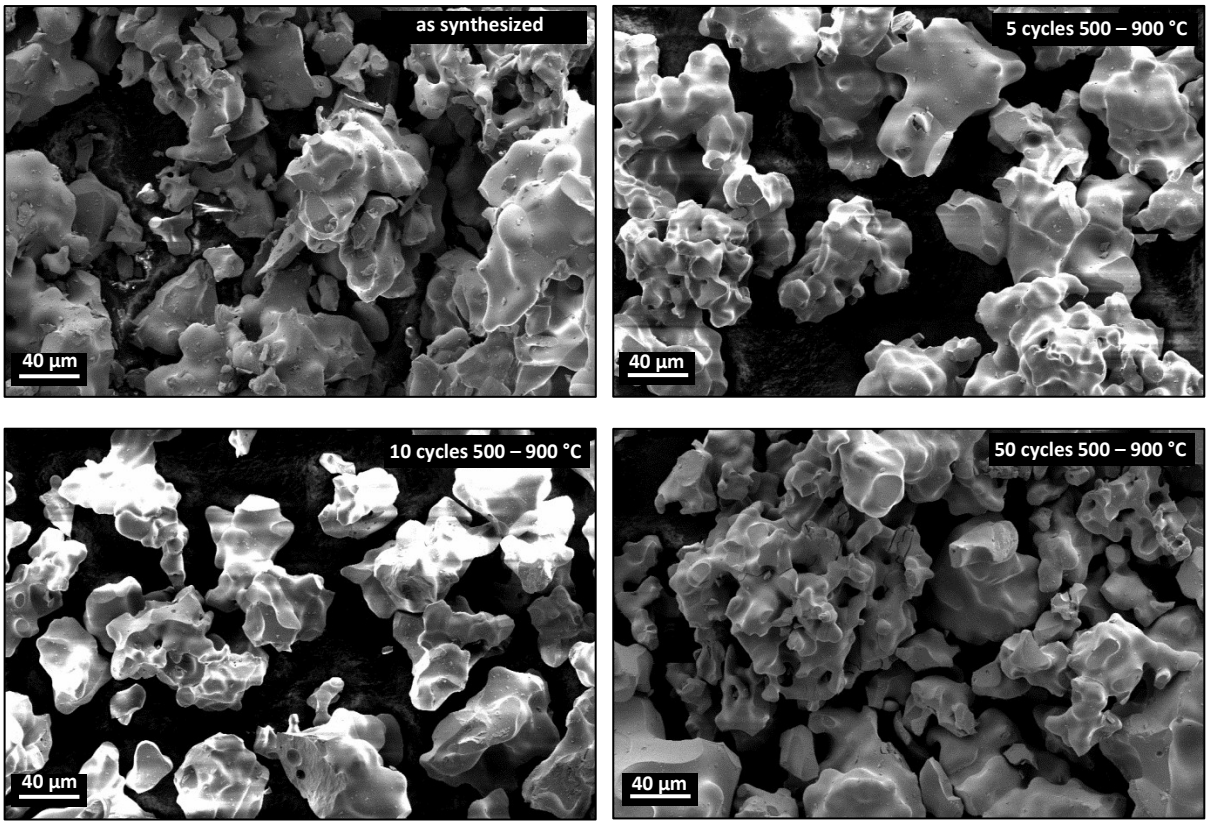

Fig. S11: SEM images of $SrFe_{0.95}Cu_{0.05}O_x$ powders after multiple redox cycles at 500 – 900 °C.

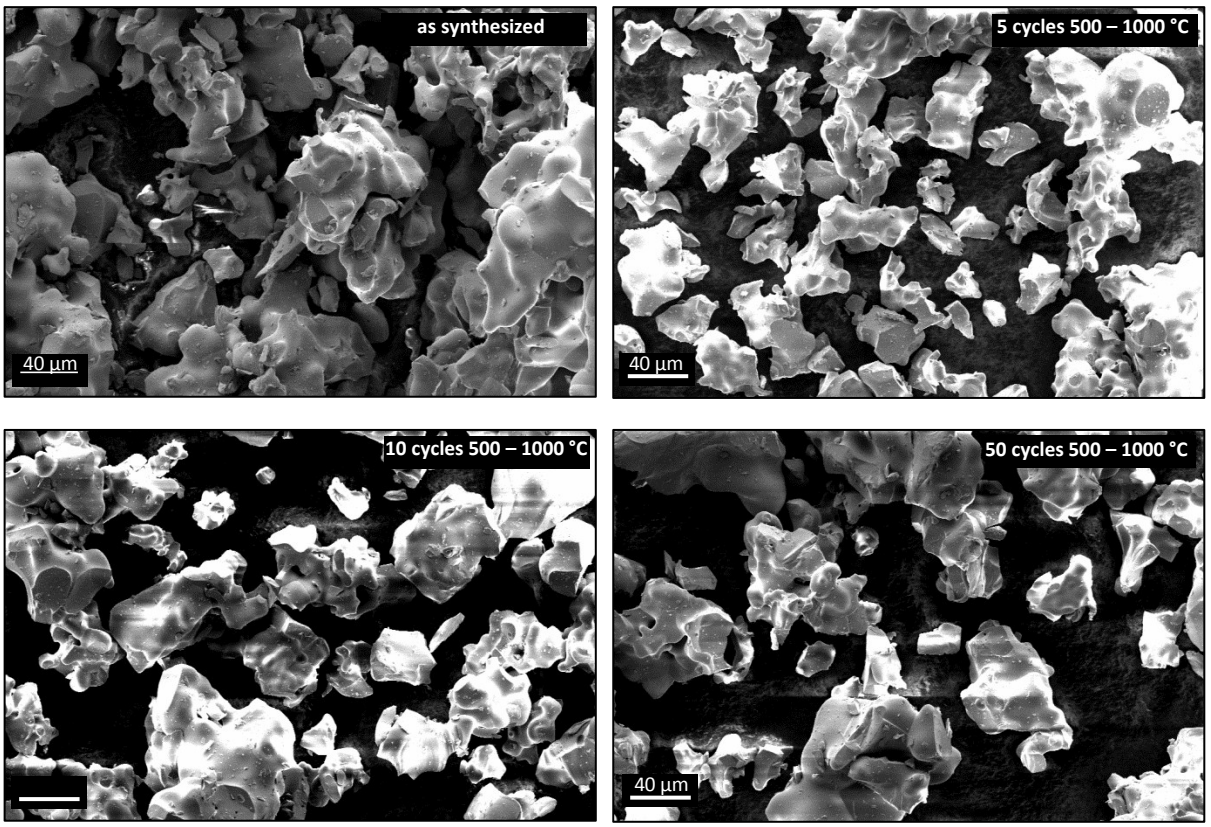

Fig. S12: SEM images of $SrFe_{0.95}Cu_{0.05}O_x$ powders after multiple redox cycles at 500 – 1000 °C.

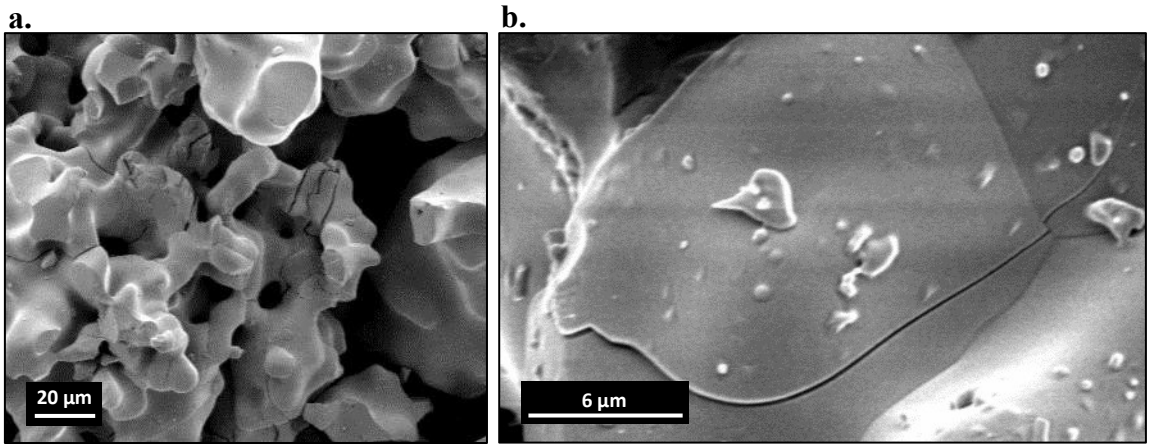

Fig. S13: Formation of cracks on a $SrFe_{0.95}Cu_{0.05}O_x$ particles **a.** after 50 redox cycles at 500 – 900 °C, **b.** after 10 redox cycles at 500 – 1000 °C.

$Ca_{0.8}Sr_{0.2}MnO_x$

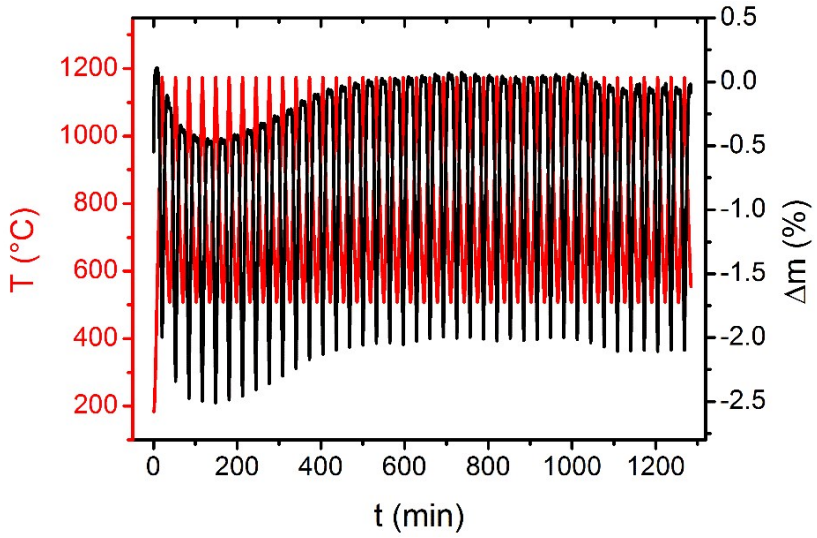

Fig. S14: Long term thermogravimetric experiment of $Ca_{0.8}Sr_{0.2}MnO_x$ at p_{O_2} = 0.16 bar. 40 redox cycles were carried out. Drift corrected linearly, no empty scan subtracted. Initial sample mass:

64.76 mg. The sample was oxidized and reduced 10 times in previous experiments. The observed non-linear drift was not corrected. The mass changes are equal throughout all redox cycles.

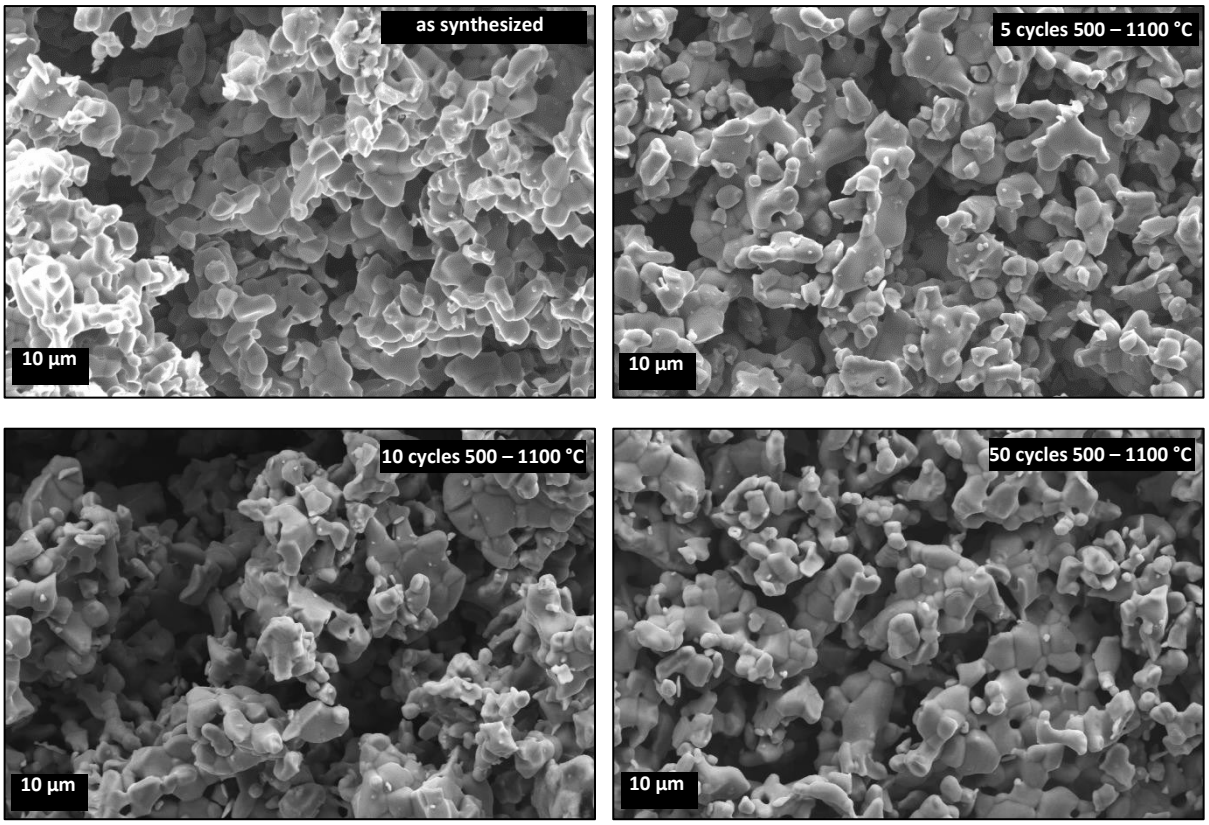

Fig. S15: SEM images of $Ca_{0.8}Sr_{0.2}MnO_x$ powders after multiple redox cycles at 500 – 1100 °C.

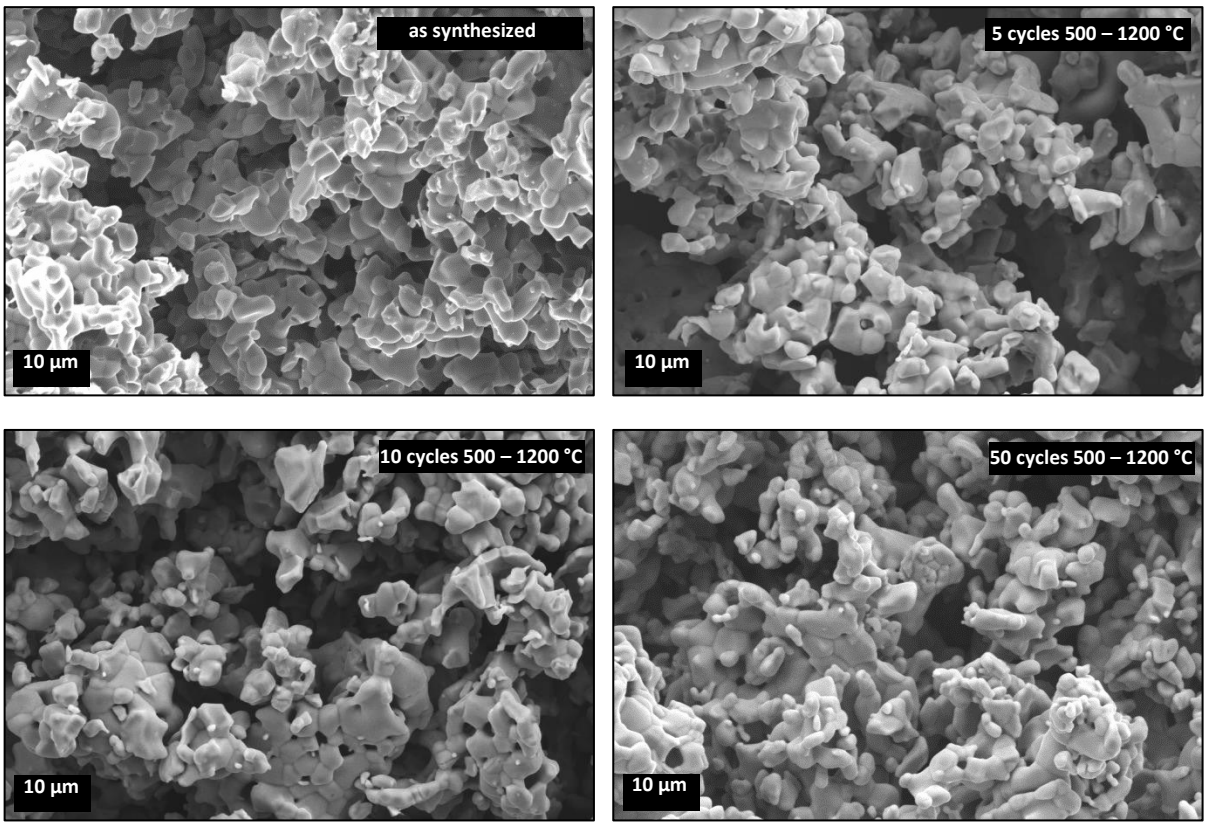

Fig. S16: SEM images of $Ca_{0.8}Sr_{0.2}MnO_x$ powders after multiple redox cycles at 500 – 1200 °C.

4. $SrCr_{0.1}Fe_{0.9}O_{3-\delta}$

Synthesis: Preparation of a mixture with composition $SrFe_{0.9}O_x$ via the citric acid auto-combustion route as described in the main article (45 mL 0.1 M $Fe(NO_3)_2$, 5 mL 5 M citric acid, 0.738 g $SrCO_3$) . After auto-combustion addition of 0.076 g Cr_2O_3 (lumps 99.6 %, Alfa Aeasar, powdered), then synthesis/calcination in open crucibles as described in the main article.

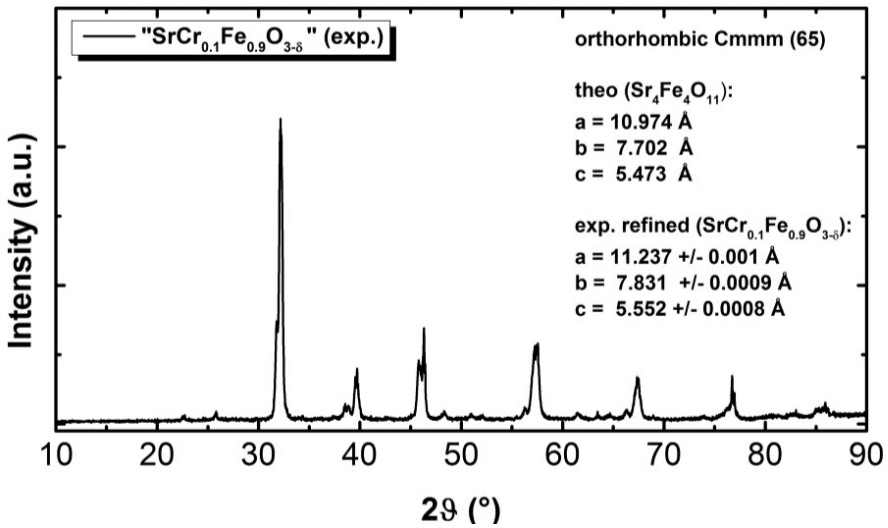

Fig. S17: Powder X-Ray diffraction pattern of Cr-doped $SrFeO_x$. Refinement performed in space group 65 with cif file No. 1521171 [1] from the *Crystallography Open Database* ($SrFeO_{2.75}$). The refined cell parameters show a large lattice expansion with respect to the undoped sample, which is attributed to a higher oxygen deficiency.

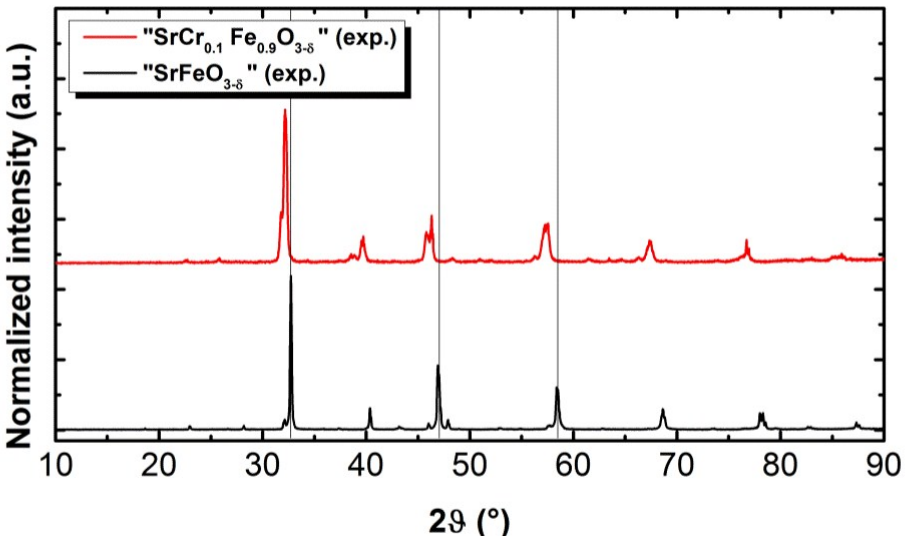

Fig. S18: Powder X-Ray diffraction pattern of Cr-doped $SrFeO_x$ compared to undoped $SrFeO_x$.

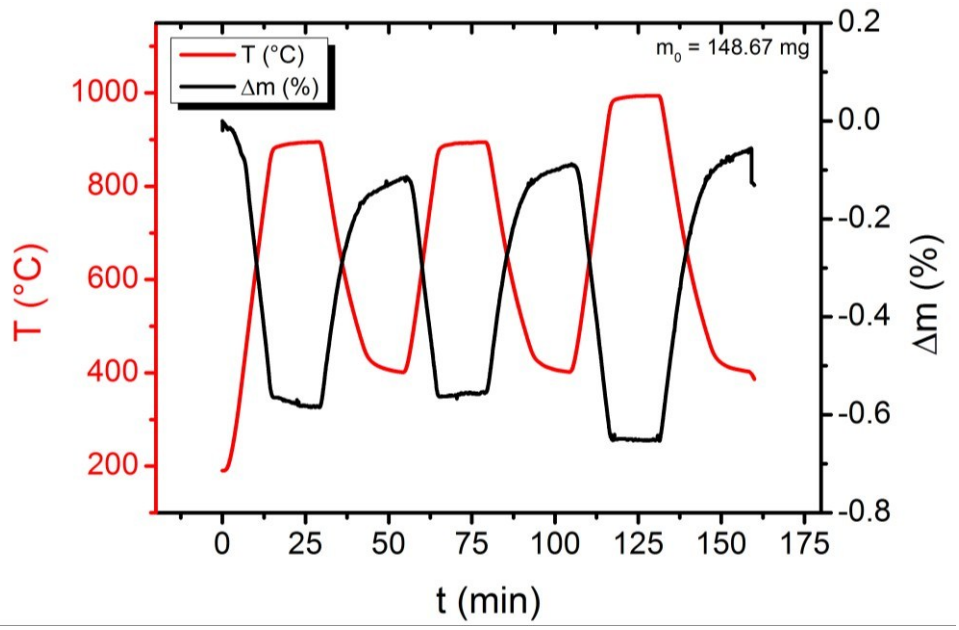

Fig. S19: Thermogravimetric analysis of $SrCr_{0.1}Fe_{0.9}O_x$ at p_{O_2} = 0.16 bar.

5. In-situ XRD $SrFe_{0.95}Cu_{0.05}O_{3-\delta}$

The reflections could be refined using an orthorhombic (space group 65, $Sr_4Fe_4O_{11}$, cif file No. 1521171 [1] from the Crystallography Open Database) or cubic unit cell. In contrary to room temperature $SrFeO_x$, at high temperatures, a cubic phase is expected to be most stable in a broad stoichiometry range. [6, 7] Therefore, the same behavior is assumed herein for the Cu-doped variant of this perovskite, and refinement is carried out in space group 221 (cubic, $SrFeO_{2.96}$, cif file No. 1528364 [8] from the Crystallography Open Database). The reflections could be indexed according to this symmetry, and it was found that the temperature dependent shift of all reflections which are visible in the full temperature range does not change the ratio between $\sin^2\vartheta$ of one reflection and $\sin^2\vartheta_{min}$ for the (100) reflection at the lowest 2ϑ value. Therefore, all these reflections can be attributed to the main phase, which exhibits an isotropic volume expansion during heat up. The derived reflection indices according to a cubic cell symmetry are shown in *Table S1.*

Table S1: Reflection indexing at 200 °C according to a cubic cell symmetry including all reflections that are visible over the full temperature range.

h	**k**	**l**	$h^2+k^2+l^2$	**2 theta**	theta	$\sin^2$theta	$\sin^2$(theta)/theta_mi
1	**0**	**0**	1	**23.00**	11.50	0.03974757	1.000
1	**1**	**0**	2	**32.75**	16.38	0.07948049	1.999
1	**1**	**1**	3	**40.40**	20.20	0.11923085	2.999
2	**0**	**0**	4	**47.40**	23.70	0.16156202	4.064
2	**1**	**1**	6	**58.47**	29.24	0.23852753	6.001
2	**2**	**0**	8	**68.65**	34.33	0.31796793	7.999
3	**1**	**0**	10	**78.17**	39.09	0.39749572	10.000

In addition to reflections that are visible over the full temperature range, at least one additional reflection is visible, which is located at ~ 45° ϑ at a temperature of 200 °C. This reflection might be attributed to impurities, most likely corresponding to those found in EDS experiments (see main article). It cannot be attributed to additional reflections appearing due to orthorhombic distortion, as the reflection position does not match with the expected positions.

This reflection could not be indexed using a cubic cell symmetry, and its temperature dependent shift was weaker than the shift of the other reflections. The shift per temperature change of all other reflections increases if T > 400 °C, which is attributed to the reduction onset. The shift of the side reflection seems to be constant at all temperatures and is therefore attributed to thermal expansion only. These facts are strong indicators for this reflection being caused by a second phase. Moreover, its intensity has a maximum around 600 °C and the reflection entirely disappeared at temperatures at 960 °C. It seems reasonable to assume that this reflection is caused by a side-phase. At high temperatures, it seems to decompose, but it forms again on cool-down, as *in-situ* XRD measurements during cool-down confirm.

6. Cell parameters in-situ XRD $Ca_{0.8}Sr_{0.2}MnO_{3-\delta}$

Table S2: Refinement in space group No. 62 (Int. Tables, *Pnma*).

T (°C)	a (Å)	a err +/-	b (Å)	b err +/-	c (Å)	c err +/-
30	5.29977	0.00501	7.5072	0.00321	5.30363	0.00453
400	5.32875	0.00433	7.52872	0.00842	5.32104	0.00568
440	5.32487	0.00399	7.53047	0.00627	5.33117	0.00477
480	5.32917	0.00406	7.53644	0.00386	5.32923	0.00464
520	5.32577	0.0047	7.54048	0.00772	5.33739	0.00337
560	5.32339	0.00191	7.5499	0.00261	5.34087	0.00169
600	5.32552	0.002	7.55424	0.00285	5.343	0.00177
640	5.33324	0.00466	7.55794	0.00627	5.34261	0.0037
680	5.33503	0.00338	7.56256	0.00428	5.34631	0.00318
720	5.34732	0.00612	7.57201	0.00425	5.34119	0.00755
760	5.35353	0.00404	7.57618	0.00432	5.34432	0.00555
800	5.36156	0.00437	7.56733	0.0045	5.35555	0.00429
840	5.36334	0.00558	7.57165	0.00484	5.36365	0.00641
880	5.36897	0.00645	7.57757	0.00432	5.36897	0.00678
920	5.3741	0.0043	7.57957	0.00256	5.37387	0.00461
960	5.36958	0.00229	7.58442	0.00203	5.38637	0.00231
1000	5.3811	0.00713	7.58827	0.0023	5.38458	0.00757
1040	5.3855	0.00871	7.59375	0.00237	5.38963	0.00905
1080	5.39488	0.00592	7.59741	0.0023	5.38777	0.00575
1120	5.40323	0.00233	7.60076	0.00175	5.39386	0.00231
1160	5.40284	0.0512	7.60333	0.00192	5.40313	0.05095
1200	5.41509	0.00365	7.6179	0.00265	5.40119	0.00359

7. Table summary of all oxides investigated

Table 3: Mass changes due to oxygen removal for all the synthesized perovskites over the various temperature ranges investigated with P_{O_2} = 0.16 bar.

Undoped $SrFeO_x$	**Temperature range**	***Δm/m***
$SrFeO_x$,	400-900 °C	0.0142
$SrFeO_x$,	400-1000 °C	0.0168
M-site doped $SrFeO_x$		
$SrCr_{0.1}Fe_{0.9}O_x$	400-900 °C	0.0045
$SrCr_{0.1}Fe_{0.9}O_x$	400-1000 °C	0.0057
$SrFe_{0.95}Cu_{0.05}O_x$	400-900 °C	0.0174
$SrFe_{0.95}Cu_{0.05}O_x$	400-1000 °C	0.0198
$SrFe_{0.92}Cu_{0.08}O_x$	400-900 °C	0.0167
$SrFe_{0.92}Cu_{0.08}O_x$	400-1000 °C	0.0188
$SrFe_{0.90}Cu_{0.10}O_x$	400-900 °C	0.0169
$SrFe_{0.90}Cu_{0.10}O_x$	400-1000 °C	0.0193
$SrFe_{0.85}Cu_{0.15}O$	400-900 °C	0.0155
$SrFe_{0.85}Cu_{0.15}O$	400-1000 °C	0.0182
$SrFe_{0.80}Cu_{0.20}O_x$	400-900 °C	0.0140
$SrFe_{0.80}Cu_{0.20}O_x$	400-1000 °C	0.0172
Undoped $AMnO_x$		
$SrMnO_x$	900-1200 °C	0.0029
$CaMnO_x$	600-1000 °C	0.0104
$CaMnO_x$	900-1200 °C	0.0176
$CaMnO_x$	600-1000 °C	0.0212
A-doped $AMnO_x$		
$Ca_{0.6}Sr_{0.4}MnO_x$	600-1000 °C	0.0123
$Ca_{0.6}Sr_{0.4}MnO_x$	900-1200 °C	0.0099
$Ca_{0.6}Sr_{0.4}MnO_x$	600-1200 °C	0.0185
$Ca_{0.7}Sr_{0.3}MnO_x$	600-1000 °C	0.0103
$Ca_{0.7}Sr_{0.3}MnO_x$	900-1200 °C	0.0123
$Ca_{0.7}Sr_{0.3}MnO_x$	600-1200 °C	0.0187
$Ca_{0.8}Sr_{0.2}MnO_x$	600-1000 °C	0.0135
$Ca_{0.8}Sr_{0.2}MnO_x$	900-1200 °C	0.0150
$Ca_{0.8}Sr_{0.2}MnO_x$	600-1200 °C	0.0232
$Ca_{0.9}Sr_{0.1}MnO_x$	600-1000 °C	0.0121
$Ca_{0.9}Sr_{0.1}MnO_x$	900-1200 °C	0.0154
$Ca_{0.9}Sr_{0.1}MnO_x$	600-1200 °C	0.0222
$Sr(Mn,Fe)O_x$		
$SrMn_{0.33}Fe_{0.66}O_x$	400-900 °C	0.0103
$SrMn_{0.33}Fe_{0.66}O_x$	400-1000 °C	0.0120
$SrMn_{0.5}Fe_{0.5}O_x$	400-900 °C	0.0074

$SrMn_{0.5}Fe_{0.5}O_x$	400-1000 °C	0.0093
$SrMn_{0.66}Fe_{0.33}O_x$	400-900 °C	0.0056
$SrMn_{0.66}Fe_{0.33}O_x$	400-1000 °C	0.0072
$Ca(Mn,Fe)O_x$		
$CaMn_{0.33}Fe_{0.66}O_x$	400-1200 °C	0.0112
$CaMn_{0.33}Fe_{0.66}O_x$	900-1200 °C	0.0030
$CaMn_{0.5}Fe_{0.5}O_x$,	400-1200 °C	0.0098
$CaMn_{0.5}Fe_{0.5}O_x$	900-1200 °C	0.0036
$CaMn_{0.66}Fe_{0.33}O_x$	400-1200 °C	0.0172
$CaMn_{0.66}Fe_{0.33}O_x$	900-1200 °C	0.0097

References

1. Hodges, J. P.; Short, S.; Jorgensen, J. D.; Xiong, X.; Dabrowski, B.; Mini, S. M.; Kimball, C. W., Evolution of Oxygen-Vacancy Ordered Crystal Structures in the Perovskite Series SrnFenO3n−1 (n=2, 4, 8, and ∞), and the Relationship to Electronic and Magnetic Properties. *Journal of Solid State Chemistry* **2000,** 151, (2), 190-209.
2. Jain, A.; Ong, S. P.; Hautier, G.; Chen, W.; Richards, W. D.; Dacek, S.; Cholia, S.; Gunter, D.; Skinner, D.; Ceder, G.; Persson, K. A., Commentary: The Materials Project: A materials genome approach to accelerating materials innovation. *APL Materials* **2013,** 1, (1), 011002.
3. Lobo, R. C.; Berry, F. J.; Greaves, C., The synthesis and structural characterization of Sr2CuO4−x, x ∼ 0.1. *Journal of Solid State Chemistry* **1990,** 88, (2), 513-519.
4. Battle, P. D.; Gibb, T. C.; Jones, C. W., The structural and magnetic properties of SrMnO3: A reinvestigation. *Journal of Solid State Chemistry* **1988,** 74, (1), 60-66.
5. Melo Jorge, M. E.; Correia dos Santos, A.; Nunes, M. R., Effects of synthesis method on stoichiometry, structure and electrical conductivity of CaMnO3−δ. *International Journal of Inorganic Materials* **2001,** 3, (7), 915-921.
6. Takeda, Y.; Kanno, K.; Takada, T.; Yamamoto, O.; Takano, M.; Nakayama, N.; Bando, Y., Phase relation in the oxygen nonstoichiometric system, SrFeOx (2.5 ≤ x ≤ 3.0). *Journal of Solid State Chemistry* **1986,** 63, (2), 237-249.
7. Mizusaki, J.; Okayasu, M.; Yamauchi, S.; Fueki, K., Nonstoichiometry and phase relationship of the SrFeO2.5SrFeO3 system at high temperature. *Journal of Solid State Chemistry* **1992,** 99, (1), 166-172.
8. Blasco, J.; Stankiewicz, J.; García, J., Phase segregation in the Gd1−xSrxFeO3−δ series. *Journal of Solid State Chemistry* **2006,** 179, (3), 898-908.